Phase-Field Model for Brittle Fracture. Validation with Experimental Results and Extension to Dam Engineering Problems

David Santillán[a,*], Juan Carlos Mosquera[a], Luis Cueto-Felgueroso[a]

[a] *Technical University of Madrid, School of Civil Engineering, C/ Profesor Aranguren 3, 28040 Madrid, Spain.*

Abstract

Phase-field formulations have recently emerged as promising tools to model brittle fracture. Based on the variational approach to fracture, these models aim at overcoming some of the computational challenges found in simulating complex fracture patterns and their evolution due to external or internal loads. Since most applications and validation exercises thus far have been restricted to academic benchmarks, the evaluation of phase-field fracture models against experimental results an practical engineering scenarios remains fragmented.

Here we introduce a straightforward phase-field approach to simulate fluid and mechanically-driven fractures based on energy minimization and thermodynamical principles. We apply our methodology to several laboratory experiments of brittle fracture, and to fracturing processes in two full-scale concrete dams, taking into account the hydraulic forces inside the fractures. We conclude that phase-field models represent a promising computational tool that may be applied to realistic engineering scenarios.

Keywords: phase-field model, fracture mechanics, laboratory experiments, dam engineering
doi.org/10.1016/j.engfracmech.2017.04.020

*Corresponding author
Email address: david.santillan@upm.es (David Santillán)

Nomenclature

$\bar{\mathbf{a}}_{\mathbf{g}}$	gravity acceleration
a	initial fracture length
B	thickness
C_f	fluid compressibility
d	phase-field variable
E	Young's modulus
$\bar{\mathbf{f}}$	body force
F	force
g_c	Griffith critical energy release rate
H^+	maximum local history field
H	height
J	J integral
K_I	stress intensity factor
K_{Ic}	toughness
ℓ	length scale parameter
L	length
$\bar{\mathbf{n}}$	unit normal vector
$\mathbf{n}_a$	principal a strain direction
p_f	pressure of fluid
q	source or sink flow rate
s	longitudinal coordinate along fracture
S	spam
t	time
$\bar{\mathbf{t}}$	applied force
$\bar{\mathbf{T}}$	traction vector
$\mathbf{u}$	displacement field
w	aperture
w/c	water to cement ratio
z	depth

γ_ℓ	fracture density
Γ	path
δ	dimension
ε	strain tensor
ε_a	principal a strain
λ	Lamé constant
μ	Lamé constant
μ_f	dynamic fluid viscosity
ν	Poisson's ratio
ρ_f	fluid density
σ	stress tensor
$\sigma_{\mathbf{0}}$	undamaged stress tensor
Ψ	total potential energy
Ψ^d	energy dissipated in the fracture process
Ψ^e	potential energy stored in the bulk of the solid
Ψ_0^e	potential energy stored in the undamaged bulk of the solid
Ψ^s	external source of energy
ψ_0^e	undamaged elastic energy density
Ω_i	i domain

D	Dirichlet boundary condition
E	elastic domain
F	fracture domain
N	Neumann boundary condition

AAT	all-around tension
CCF	configuration correction factor
CPC	crack-parallel compression
PPMA	polymethyl methacrylate
UNI	uniaxial loading

$g(\cdot)$	degradation function

$\nabla \cdot \mathbf{F}$	divergence of vector field $\mathbf{F}$
∇f	gradient of scalar field f
$\nabla^2 f$	Laplacian of scalar field f
$\lvert a \rvert$	modulus of scalar a
$\lVert \mathbf{b} \rVert$	norm of vector $\mathbf{b}$
$\mathbf{b} \otimes \mathbf{c}$	tensor product of $\mathbf{b}$ and $\mathbf{c}$

1. Introduction

Fracture is one of the most important failure mechanisms of structures. Reliable and efficient fracture models play a vital role in the safety assessment of civil engineering structures such as bridges, tunnels or dams. In particular,

large dams are of special concern for engineers due to the high potential risk in case of total destruction, as reported for some catastrophic events [1], or the economic and environmental losses associated to a quick reservoir lowering due to a partial failure. Moreover, the estimates of dam failure probabilities for specific failure modes, e.g. sliding along the rock-concrete interface [2], or the structural safety evaluation against future larger thermal loads due to the climate change [3, 4], are current research topics. Dam risk analysis requires numerical modeling tools capable of simulating failure modes, among which the prediction of both fracture initiation and propagation are of great importance.

Numerical models for fracture mechanics can be classified into two main categories, namely discrete and continuous approaches. Fractures are simulated as discontinuities in the discrete approaches. The simplest way to model discontinuities includes splitting nodes [5], or breaking elements [6]. However, two drawbacks of these methods are the change of the topology of the discretization and the restriction of the fracture propagation to follow mesh lines. These limitations can be partially overcome by remeshing techniques [7] or using advanced approaches.

New discrete advanced approaches include the so-called cohesive zone modeling or the enriching displacement field methods. The former simulates discontinuities through laws that relate traction to displacement jumps [8] and fractures are typically coincident with element sides. The latter approach locates discontinuities inside the finite elements whose formulation is enriched with additional discontinuous displacement modes [9, 10]. The enrichment can be modal, denoted as X-FEM, or elemental, called E-FEM, with similar performance [11].

Continuous approaches describe the intact solid and fracture domains as a single continuum. These models are computationally appealing, as they retain geometric simplicity and straightforward discretization in the context of e.g. standard finite element methods. A relatively recent continuous approach is the phase-field model, in which fractures are regularized using an auxiliary scalar variable, the phase-field, which smears the discontinuity and interpolates between the broken and unbroken areas. The major advantages of using phase-field models are [12]: (1) the approach is fixed-mesh, (2) the formulation is based on energy minimization and, consequently, nucleation, propagation or fracture path are automatically computed without the need to track algorithmically fractures, (3) fracture joining or branching do not need for additional algorithms, and (4) fracture propagation in heterogeneous media can be simulated without any additional modification in the computational framework. The main drawbacks of phase-field models are: (1) the computational mesh has to be small enough to capture the physics and the characteristic lengths of the fracture problem, and (2) since broken regions are modeled as a diffused field, fracture paths must be recovered from that field.

Phase-field models for fracture mechanics can be classified into two families. The first emerged within the physics community inspired in the work of *Aranson et al.* [13], who proposed a continuum-field model for mode-I fracture propagation in brittle amorphous solids. This idea has been further developed by many authors, such as *Karma et al.* [14], *Eastgate et al.* [15], *Henry and Levine*

[16], *Karma and Lobkovsky* [17], or *Spatschek et al.* [18].

The second family emerged in the mechanics community on the basis of the works of *Ambrosio and Tortorelli* [19], who proposed a phase-field approximation of the Mumford-Shah potential [20] based on the Γ-convergence. Inspired on these works, *Francfort and Marigo* [21] proposed a variational formulation for brittle fracture based on energy minimization of the combined elastic and fracture energies. The numerical implementation was developed by *Bourdin et al.* [22], which defined the phase-field variable that distributes the fracture energy over the solid. In practical implementations, both families yield relatively similar numerical schemes [23].

An alternative quasi-static formulation of this phase-field approximation has been proposed by *Miehe et al.* [24], and applied to brittle fracture based on continuum mechanics and thermodynamical principles. This framework has been extended to dynamic problems [25, 26, 27], coupled to thermo-mechanical effects at large strains [28], and adapted to simulate ductile fracture coupled with thermo-plasticity at finite strains [29]. In addition, phase-field models have been extended to simulate cohesive fracture [30], fluid-driven fracture [31, 32], or electromechanical-driven fracture [33], and combined with structural models such as plates and shells [34]. The performance of phase-field models to simulate fluid-driven fracturing in elastic media has been assessed against analytical solutions under different fracture propagation regimes with encouraging results [35].

Most phase-field models of fracture have thus far been applied to academic benchmarks alone. The validation of phase-field formulations using experimental observations, and their applicability to practical engineering problems, remains an open research problem. Here, we evaluate whether phase-field models can be considered as an alternative to simulate fracture propagation in realistic structures. Our work aims to translate the phase-field approach to the engineering practice, and we argue that it indeed represents a promising future tool. We introduce a relatively straightforward phase-field approach to model fluid and mechanical-driven brittle fracture based on energy minimization and thermodynamical principles. We simulate several laboratory experiments of brittle fracture and compare our results with the experimental ones. We also apply the model to simulate the fracture of two full-scale concrete dams, where the effect of hydraulic pressure inside the fracture is also accounted for under suitable simplifying assumptions.

The paper is organized as follows: the mathematical formulation of the model is described in section 2. In section 3 we introduce some laboratory experiments collected from the literature, simulate and compare the experiments with the results of the phase-field model simulations. In section 4 we apply a phase-field model to simulate the fracture of two full-scale concrete dams. Finally, conclusions are reported in section 5.

2. Governing equations

In this section, we derive the mathematical model for brittle fracturing. First, we describe the geometry of the problem. Then, we derive the mechanical formulation and fracture propagation equations from variational principles. The mechanical effects from pressure fluid inside the fracture are accounted for. Afterward, we introduce some remarks for the numerical implementation of the model. Finally, we describe the J integral analysis.

2.1. Geometry

Let us consider the geometry depicted in Fig. 1, where the domain $\Omega \subset \Re^{\delta}$ has dimension $\delta \in \{2, 3\}$. The solid is composed of an impermeable elastic subdomain Ω_E and a fracture subdomain Ω_F, whereby $\Omega = \Omega_E \cup \Omega_F$. The boundary of Ω_i is denoted by $\partial_k \Omega_i$, where the subscript $i = E, F$ refers to each subdomain, and $k = D, N$ is introduced in allusion to the type of boundary condition, Dirichlet or Neumann respectively. The unit normal vector to Ω is $\bar{\mathbf{n}}$. In addition, Ω_F can be filled with fluid, which exerts a force over Ω_E.

2.2. Variational formulation to brittle fracture

Our formulation adopts the Griffith energy-based failure criterion to model fracture propagation. The criterion relies on linear elastic fracture mechanics and states that the elastic energy released during the fracture propagation process is balanced by newly created surface energy [36]. This interpretation was adopted by *Francfort and Marigo* [21] to develop a variational approach formulation for brittle fracture based on the minimization of the total potential energy stored in the solid Ψ.

Ψ is the sum of three components: the energy dissipated in the fracture process Ψ^d, the energy stored in the bulk of the solid Ψ^e, and the external sources of energy Ψ^s,

$$\Psi = \Psi^d + \Psi^e - \Psi^s. \tag{1}$$

Ψ^d is the work required to create a unit fracture area,

$$\Psi^d = \int_{\partial\Omega_F} g_c \, \mathrm{d}\partial, \tag{2}$$

where g_c is the Griffith critical energy release rate for mode I failure. The regularization of the fracture surface allows to extend Eq. (2) over the whole domain Ω as follows:

$$\Psi^d = \int_{\Omega} g_c \gamma_\ell \, \mathrm{d}\Omega, \tag{3}$$

where γ_ℓ is the fracture density given by [24]:

$$\gamma_\ell = \frac{1}{2\ell} d^2 + \frac{\ell}{2} \left| \nabla d \right|^2, \tag{4}$$

ℓ is the length scale parameter, and d is the phase-field variable which interpolates between the broken and sound regions of the solid where $d = 1$ and $d = 0$ respectively.

The elastic energy stored in the undamaged bulk of the solid, Ψ_0^e, is defined as

$$\Psi_0^e = \int_\Omega \psi_0^e(\varepsilon)\, \mathrm{d}\Omega, \tag{5}$$

where ψ_0^e is the undamaged elastic energy density, given by:

$$\psi_0^e(\varepsilon) = \frac{\lambda}{2}\mathrm{tr}(\varepsilon)^2 + \mu \mathrm{tr}(\varepsilon^2), \tag{6}$$

λ and μ are the Lamé constants, ε is the infinitesimal strain tensor, $\varepsilon = \frac{1}{2}\left(\nabla \mathbf{u} + \nabla \mathbf{u}^T\right)$, and $\mathbf{u}$ is the displacement field.

The fracture propagation degrades Ψ_0^e due to the loss of stiffness. From a mathematical point of view, the degradation process can be modeled through two approaches [24]: the *isotropic* formulation, where the elastic energy degrades regardless of the sign of strain, or the *anisotropic* formulation which assumes degradation in tension only. We adopt the latter, as it is more realistic for concrete and geomaterials. The damaged elastic energy, Ψ^e, is then given by

$$\Psi^e = \int_\Omega \left[g(d)\psi_0^{e+}(\varepsilon) + \psi_0^{e-}(\varepsilon) \right] \mathrm{d}\Omega = \int_\Omega \psi^e(\varepsilon, d)\, \mathrm{d}\Omega, \tag{7}$$

where ψ_0^{e+} is the part of the undamaged elastic energy generated by tension, ψ_0^{e-} the energy generated by compression, and $g(d)$ is the degradation function which is commonly defined as $g(d) = (1-d)^2$ [37]. Tension/compression components of the undamaged energy read

$$\psi_0^{e\pm}(\varepsilon) = \frac{\lambda}{2}\left(\left\langle \sum_{a=1}^{\delta} \varepsilon_a \right\rangle_\pm \right)^2 + \mu \sum_{a=1}^{\delta} \left(\langle \varepsilon_a \rangle_\pm \right)^2, \tag{8}$$

where ε_a is the a-th principal strain, δ is the dimension of the problem, and $\langle x \rangle_\pm = (x \pm |x|)/2$. The above decomposition satisfies $\psi_0^e(\varepsilon) = \psi_0^{e+}(\varepsilon) + \psi_0^{e-}(\varepsilon)$. The corresponding Cauchy stress tensor, incorporating damage, is given by:

$$\sigma(\mathbf{u}, d) := g(d)\frac{\partial \psi_0^{e+}}{\partial \varepsilon} + \frac{\partial \psi_0^{e-}}{\partial \varepsilon}, \tag{9}$$

or, alternatively

$$\sigma^+(\mathbf{u}, d) = g(d) \sum_{a=1}^{\delta} \left[\lambda \left\langle \sum_{i=1}^{\delta} \varepsilon_i \right\rangle_+ + 2\mu \langle \varepsilon_a \rangle_+ \right] \mathbf{n}_a \otimes \mathbf{n}_a, \tag{10}$$

for positive stress –tension–, and

$$\sigma_0^-(\mathbf{u}) = \sigma^-(\mathbf{u}) = \sum_{a=1}^{\delta} \left[\lambda \left\langle \sum_{i=1}^{\delta} \varepsilon_i \right\rangle_- + 2\mu \langle \varepsilon_a \rangle_- \right] \mathbf{n}_a \otimes \mathbf{n}_a, \tag{11}$$

for negative stress –compression–, where $\mathbf{n}_a$ is the principal strain direction associated to the principal strain ε_a. The eigenvalue bases, $\mathbf{n}_a \otimes \mathbf{n}_a$, are computed in terms of the principal strains, ε_i, with $i = a, b$, and the strain tensor, ε, as follows [38]:

$$\mathbf{n}_a \otimes \mathbf{n}_a = \frac{1}{\prod_{b \neq a}^{\delta} (\varepsilon_a - \varepsilon_b)} \prod_{b \neq a}^{\delta} (\varepsilon - \varepsilon_b \mathbf{1}) \,. \tag{12}$$

Eq. (12) is only valid when all eigenvalues are different. In the particular case where all three eigenvalues are equal, any direction is an eigenvector. The stress field is then isotropic. In case that two eigenvalues are equal and the third is different, the eigenvectors corresponding to the former eigenvalues can be in any orthogonal directions in a plane, and the third eigenvector is normal to that plane.

The external energy functional, Ψ^s, accounts for the exchange of energy between the elastic subdomain, Ω_E, and the surrounding environment and reads:

$$\Psi^s = \int_{\Omega} \overline{\mathbf{f}} \cdot \mathbf{u} \, \mathrm{d}\Omega + \int_{\partial_N \Omega_E} \overline{\mathbf{t}} \cdot \mathbf{u} \, \mathrm{d}\partial, \tag{13}$$

where $\overline{\mathbf{f}}$ is the body force per unit volume, $\overline{\mathbf{t}}$ is the vector of applied traction surface forces, and $\mathbf{u}$ is the displacement field. The second term on the right-hand side of Eq. (13) includes the force exerted by the fluid pressure inside the fracture, p_f:

$$\int_{\partial_N \Omega_E} \overline{\mathbf{t}} \cdot \mathbf{u} \, \mathrm{d}\partial = \int_{\partial_N \Omega} \overline{\mathbf{t}} \cdot \mathbf{u} \, \mathrm{d}\partial - \int_{\partial_N \Omega_F} p_f \bar{\mathbf{n}} \cdot \mathbf{u} \, \mathrm{d}\partial. \tag{14}$$

The second term of Eq. (14) is a flux of energy through the surface of the fracture. By using the divergence theorem, we rewrite it as

$$\int_{\partial_N \Omega_F} p_f \bar{\mathbf{n}} \cdot \mathbf{u} \, \mathrm{d}\partial = \int_{\Omega_E} \nabla \cdot (p_f \mathbf{u}) \, \mathrm{d}\Omega - \int_{\partial_N \Omega_E} p_f \bar{\mathbf{n}} \cdot \mathbf{u} \, \mathrm{d}\partial, \tag{15}$$

where the work associated to the pressure force applied on the fracture surface is now defined as a integral extended over the entire elastic subdomain. Nevertheless, Ω_E changes with time due to the fracture propagation. We avoid this drawback by introducing the aforementioned degradation function, $g(d)$, which allows us to redefine the integral over the entire domain [39]:

$$\int_{\Omega_E} \nabla \cdot (p_f \mathbf{u}) \, \mathrm{d}\Omega - \int_{\partial_N \Omega_E} p_f \bar{\mathbf{n}} \cdot \mathbf{u} \, \mathrm{d}\partial = \int_{\Omega} g(d) \nabla \cdot (p_f \mathbf{u}) \, \mathrm{d}\Omega - \int_{\partial_N \Omega} g(d) p_f \bar{\mathbf{n}} \cdot \mathbf{u} \, \mathrm{d}\partial. \tag{16}$$

Therefore, the external energy functional finally reads:

$$\Psi^s = \int_{\Omega} \overline{\mathbf{f}} \cdot \mathbf{u} \, \mathrm{d}\Omega - \int_{\Omega} g(d) \nabla \cdot (p_f \mathbf{u}) \, \mathrm{d}\Omega + \int_{\partial_N \Omega} g(d) p_f \bar{\mathbf{n}} \cdot \mathbf{u} \, \mathrm{d}\partial + \int_{\partial_N \Omega} \overline{\mathbf{t}} \cdot \mathbf{u} \, \mathrm{d}\partial, \tag{17}$$

We derive the strong form of the problem via minimization of the total potential energy, Ψ, with respect to the displacement, $\mathbf{u}$, and phase-field variable, d. The Fréchet derivative of Ψ with respect to $\mathbf{u}$ yields the mechanical equilibrium equations, which in terms of the positive and negative stress contributions reads:

$$\nabla \cdot \left\{ g(d)\sigma_0^+ + \sigma_0^- \right\} + p_f \nabla g(d) + \bar{\mathbf{f}} = \mathbf{0}, \quad \text{in } \Omega, \tag{18}$$

$$\sigma \bar{\mathbf{n}} = \bar{\mathbf{t}} + g(d) p_f, \quad \text{in } \partial_N \Omega. \tag{19}$$

The Fréchet derivative of Ψ with respect to d provides the Euler equations of the phase-field problem:

$$\frac{g_c}{\ell} \left(d - \ell^2 \nabla^2 d \right) = 2(1-d) \left(\psi_0^{e+}(\varepsilon) + p_f \nabla \cdot \mathbf{u} + \mathbf{u} \cdot \nabla p_f \right), \quad \text{in } \Omega, \tag{20}$$

$$\nabla d \cdot \bar{\mathbf{n}} = 0, \quad \text{in } \partial_N \Omega. \tag{21}$$

A straightforward way to account for the irreversibility of the fracture process is introducing the maximum local history field H^+, defined as [40]:

$$H^+(\mathbf{u}, p_f, t) = \max_{s \in [0,t]} \left(\psi_0^{e+}(\varepsilon) + p_f \nabla \cdot \mathbf{u} + \mathbf{u} \cdot \nabla p_f \right), \tag{22}$$

and the Euler equation of the phase-field is then written as:

$$\frac{g_c}{\ell} \left(d - \ell^2 \nabla^2 d \right) = 2(1-d) H^+. \tag{23}$$

2.3. Some remarks regarding the numerical implementation

The governing equations of the problem are the equilibrium and phase-field equations, plus a third equation that describes the fluid motion inside the fracture, which is written in terms of the fluid pressure. The first one reads

$$\nabla \cdot \{\sigma\} + p_f \nabla g + \bar{\mathbf{f}} = \mathbf{0}, \tag{24}$$

where the stress tensor σ is given by

$$\sigma = g(d)\sigma_0^+ + \sigma_0^-, \tag{25}$$

and

$$\sigma_0^{\pm} = \lambda \left(\mathrm{tr}(\varepsilon) \right)^{\pm} \mathbf{I} + 2\mu \varepsilon^{\pm}. \tag{26}$$

Under plane strain conditions, the Lamé constants are

$$\lambda = \frac{\nu E}{(1+\nu)(1-2\nu)}, \quad \mu = \frac{E}{2(1+\nu)}, \tag{27}$$

whereas under plane stress conditions they are

$$\lambda = \frac{\nu E}{(1+\nu)(1-\nu)}, \quad \mu = \frac{E(1+2\nu)}{3(1+\nu)(1-\nu)}. \tag{28}$$

In the above expressions, ν is the Poisson's ratio, and E is the Young's modulus.

The phase-field equation can be written as:

$$\frac{g_c}{\ell}\left(d - \ell^2 \nabla^2 d\right) = 2(1-d)H^+. \tag{29}$$

where H^+ is given by Eq. (22).

Fluid flow inside the fracture is commonly assumed to be laminar, and the pressure p_f is assumed to evolve according to the Reynolds' lubrication equation, which reads:

$$\frac{\partial w}{\partial t} + C_f w \frac{\partial p_f}{\partial t} = \nabla_s \cdot \left(\frac{w^3}{12\mu_f} \left(\nabla_s p_f - \rho_f a_g \nabla_s z \right) \right) + q, \quad \text{in } \Omega_F, \tag{30}$$

where w is the fracture aperture, C_f is the fluid compressibility, a_g is the gravity acceleration, z is the depth, s is the longitudinal coordinate along the fracture, and q is a source or sink. The fracture flow equation (30) has a lower dimensionality in space and its domain follows the fracture path. The fracture domain is defined as an entity in which the gradient of the phase-field is zero and the phase-field variable is above a threshold d_f.

The aperture at any point $\mathbf{x}$ along the fracture is evaluated through the line integral [39]

$$w(\mathbf{x}) = \int_a^b \mathbf{u}(r(\eta)) \cdot \nabla d(r(\eta)) \, \|r'(\eta)\| \, \mathrm{d}\eta, \tag{31}$$

where $r(\eta)$ is the line normal to the fracture that passes through $\mathbf{x}$. The integral (31) is truncated to the interval $[\mathbf{r}(a), \mathbf{r}(b)]$, whose limits denote points that are far enough from the fracture so that $\nabla d(\mathbf{r}(a))$ and $\nabla d(\mathbf{r}(b))$ are negligible

The mechanical effect of the fluid pressure along the fracture is accounted for through the term $p_f \nabla \cdot g(d)$ in the equilibrium equation. The surface force exerted by the fluid pressure at the fracture walls is transformed into an equivalent body force applied in the whole domain. Moreover, since the phase-field variable decays exponentially away from the fracture, the degradation function $g(d)$ concentrates the effect of the pressure at the fracture. The conversion from surface to body force requires the definition of a "fictitious" pressure field over the whole domain in which, for an impermeable solid, the pressure of the closest point at the fracture is assigned to the points in the elastic domain.

We assume the fracture propagates in the *toughness dominated* regime [41], which means that the energy expended in fracturing the solid is much larger than the viscous dissipation. Consequently, the head loss caused by the fluid motion inside the fracture is negligible, so there is no need to solve Eq. (30) since p_f equals the hydrostatic head.

Eqs. (24)-(29) constitute a coupled nonlinear system of partial differential equations. The equilibrium equation (24) includes a nonlinear stress-strain relation due to the spectral decomposition of the strain tensor and the presence of the phase-field variable though the degradation function. However, the equation can be linearized by using the so-called *hybrid* formulation for the stress-strain

relationship [23], along with a staggered scheme for computing the displacement field $\mathbf{u}$, and the phase-field d [40].

The hybrid formulation retains a linear equilibrium equation within a staggered algorithm for computing d. The formulation involves the *isotropic* stress–strain relationship

$$\sigma(\mathbf{u}, d) := g(d) \frac{\partial \psi_0^e}{\partial \varepsilon} \tag{32}$$

as well as the phase-field equation (29), where the evolution of d is only driven by the tensile energy ψ_0^{e+}. The interpenetration of solid at both sides of the fracture is avoided by imposing the constraint

$$\forall\ \mathbf{x} \quad : \quad \Psi_0^{e+} < \Psi_0^{e-} \quad \Rightarrow \quad d := 0. \tag{33}$$

in the phase-field equation (29). The hybrid formulation provides similar results to those of the anisotropic formulation with lower computational effort [23]

Miehe et al. [40] proposed a staggered scheme for computing $(\mathbf{u}; d)$, which is a simple and robust alternative to the monolithic one. Nevertheless, the scheme requires sufficiently small loading increments to properly capture the non-linearity and strong coupling of the problem. A single step of the staggered scheme in the time interval $[t_n; t_{n+1}]$ is composed of these substeps:

1. The displacement, fracture phase, fracture pressure, and maximum historical energy fields $\mathbf{u}_n$, d_n, p_{fn}, and H_n^+ are known. Update the prescribed load at time t_{n+1}.
2. Update H^+ with the values of the fields at time t_n.
3. Compute the phase-field d with the updated H^+.
4. Determine the displacement field $\mathbf{u}$ at frozen phase-field d computed in the previous step.

We adopt the staggered scheme of *Miehe et al.* [40], but we compute the displacement and fracture phase fields $\mathbf{u}$ and d with a coupled scheme. Although the formulation is quasi-static, the prescribed loads are time-dependent. We adopt a fully implicit and adaptive time integration, based on backward differentiation formulae [42]. At each time step, the nonlinear solver performs damped Newton iterations until the solution is converged to a certain tolerance. The time step required to solve unstable fracture growth is typically below a microsecond.

2.4. Approach to J integral

The energy release rate, g_c, can be expressed in terms of the so-called stress intensity factor, K_I [43]. K_I characterizes the stress field in the region around to a sharp crack tip [44], and thereby it provides a way to discern if a fracture will propagate. The J integral is a method to characterize the stress-strain field at the crack tip of a 2D domain. *Rice* [45] defined it as a 2D energy line integral that can be used to infer the fracture tip behavior when the stress field away from the tip can be assessed through elastic analysis. It is given by:

$$J = \int_\Gamma \left(\psi_0^e(\varepsilon)\, \mathrm{d}x_2 - \bar{\mathbf{T}} \cdot \frac{\partial \mathbf{u}}{\partial x_1}\, \mathrm{d}s \right), \tag{34}$$

where Γ is a curve surrounding the fracture tip, (x_1, x_2) are the coordinate directions, being the fracture surfaces parallel to the 1-axis, $\bar{\mathbf{T}}$ is the traction vector defined to the outward normal along Γ, $T_i = \sigma_{ij} n_j$, and ds is an element of arc length along Γ. The integral is evaluated counterclockwise over Γ.

The J integral concept is suitable for materials that undergo small-scale yielding at the crack tip, *i.e.* the plastic zone size is small compared to the fracture length and the geometric dimensions. Hence, the integral is a way to extend fracture-mechanics concepts from linear elastic behavior to elastic-plastic [44]. *Rice* [45] proved the path-independence of the line integral, and stated that for small-scale yielding the J integral is identical to g_c. Therefore, the J integral is related to the stress intensity factor K_I for plane strain by:

$$J = g_c = \frac{K_I^2}{E} \left(1 - \nu^2\right), \tag{35}$$

and for plane stress by:

$$J = g_c = \frac{K_I^2}{E}. \tag{36}$$

3. Laboratory experiments

In this section we describe two laboratory experiments whose results are available in the literature. The first one investigates the two-dimensional propagation path of fractures in polymethyl methacrylate (PPMA) plates subjected to different biaxial loading states [46]. The second one studies the failure of mortar specimens subjected to three point bending test [47]. We simulate both experiments and compare our numerical results with the experimental ones.

3.1. PPMA plates subjected to biaxial loading state

Thomas and Pollard [46] investigated the two dimensional propagation path of fractures in PMMA plates as function of both the applied biaxial loading and the initial geometry of a fracture array. The experiment layout is depicted in Fig. 2a. A 4.5 mm thick cross-shape PPMA plate was subjected to imposed normal displacements at the arms of the cross. Two narrow parallel starter slots of 6.16×0.16 cm were milled near the center of the plate. Both slots are depicted in black solid line in the figure. They are located inside a dashed line rectangle, the region within which fractures are supposed to propagate. The slots centers had a parallel separation of 19.0 cm and three perpendicular spacings were tested, 1.0, 3.0, and 6.0 cm. Small cracks 3 ± 1 mm in length were notched into the inner tips of the started slots. Here, we only consider the experiments with 6.0 cm perpendicular spacing. The mechanical properties of the PPMA plastic are: Young's modulus $E = 3.10$ GPa, Poisson's ratio $\nu = 0.38$, and fracture toughness $K_{IC} = 1.56$ MPa$\cdot$m$^{1/2}$.

Three loading cases were considered and two experiments were conducted for each case -Fig. 2c first row-. The loads were applied by prescribing displacements at the boundaries, providing conditions of all-around tension (AAT), uniaxial

loading (UNI), and crack-parallel compression (CPC), respectively. The authors report that fractures randomly propagate from only one of the two slots.

Our computational mesh is depicted in Fig. 2b. The central rectangle of 28×8 cm is meshed by 4-noded regular square elements with size of 0.5 mm. The mesh is then composed of $32,478$ triangular elements and $88,948$ square elements. The remaining domain is meshed by 3-noded free triangular elements with maximum size of 1.1 cm. We introduce the starter slots as holes in the domain and we allow the fracture to propagate from only one of the initial slots. Moreover, we assume plane stress conditions. The fracture energy is then given by $g_c = K_{IC}^2/E$ [43].

The simulations are run on a machine with an Intel Core i5-2400 CPU @ 3.10 GHz processor and 32 Gb RAM memory. The computational time varies from $30,408$ s for the CPC experiment to $53,324$ s for the AAT case. The minimum time step is reached during the unstable growth phase of the fracture, and varies from 6.25×10^{-13} s in the AAT simulation to 3.20×10^{-8} s in the CPC case. Although the AAT experiment requires the largest critical displacements, this simulation is computationally the most demanding because of the required extremely small time step.

Both our numerical results of fracture paths and the experimental results are plotted for comparison in Fig. 2c. Below the scheme of each load case, the first row schematically provides the experimental results extracted from [46], the second row includes the contour plots of the phase field variable of our numerical results, and the last row contains the diagrams of force-deflections for our numerical simulations.

The first column includes the case of all-around tension (AAT), *i.e.*, the applied displacements at the four cross arms are outward with the same magnitude. Two patterns were obtained in the experiments: in the first one, the fracture propagates from the lower slot following a straight path and halfway it turns and joins with the opposite slot. By contrast, in the second pattern the fracture turns halfway but it does not join with the slot. The agreement between our numerical results and the first pattern is remarkable. Nevertheless, our model is not able to reproduce the second path.

Thomas and Pollard [46] also conducted numerical simulations to reproduce their experimental results. The authors were only able to reproduce one of the trajectories. Since the employed numerical models are deterministic, we attribute the inability to reproduce both paths to the fact that the results from laboratory experiments may have randomness components. Such randomness can arise from the fact that materials are not completely homogeneous, the practiced notches are not exactly equal, or the imposed displacements in the boundaries are not perfectly equal each other, among other sources.

The second column depicts an uniaxial (UNI) loading case. The experiments show the fracture propagates from the lower slot following a straight path and it slightly turns due to the influence of the upper slot. Our numerical simulations accurately match this pattern.

The third column plots a crack-parallel compression (CPC) loading case. The prescribed displacement perpendicular to slots generates tension, while the

parallel ones produces compression. The absolute magnitude of the four displacements is the same. The experiments show that the fracture propagates from the lower slot by following a straight path, and due to the compression generated by the imposed parallel prescribed displacements to slots, the fracture does not turn as in the previous case. Our numerical simulation matches with experimental results.

Below each contour plot of phase-field variable, we provide the evolution of the imposed normal displacements in the boundaries against the reaction forces. The relationship between both variables is linear until the critical displacement is reached. Then, a sudden decrease in the forces occurs due to the fast propagation of the fracture. The maximum reaction force is different in each experiment. The largest peak force is given in the AAT experiment, and the lowest in the CPC experiment. We attribute this to the imposed horizontal displacements. In the first case, the horizontal displacement tends to produce compression in the perpendicular direction due to the effect of Poisson's ratio and it counteracts the tension generated by the vertical displacement. Instead, in the last experiment the consequences of the horizontal displacement is the opposite, it generates tension in the perpendicular direction. The UNI experiment represents an intermediate situation where no horizontal displacement is imposed.

3.2. Mortar specimens subjected to three point bending test

Ge et al. [47] proposed a phase-field model inspired in the philosophy of the physic community to simulate quasi-brittle fracture behavior of mortar. The starting point for the formulation was the Ginzburg-Landau form of total energy in the system, and the evolution of the phase-field variable was simulated through the Allen-Cahn dynamic equation. The authors modified this equation by adding a white noise term to simulate the quasi-brittle fracture behavior. The model was verified by conducting a three-point bending laboratory test of mortar specimens.

A schematic setup of the laboratory experiments is provided in Fig. 3a. The beams had a height H of 40 mm, a thickness B of 20 or 40 mm, a length L of 160 mm, and a spam S of 130 mm. A initial notch was placed in the center of the span whose dimensions were 2 mm thickness and four different lengths a were considered: 10, 12.5, 15, and 17.5 mm. Two water-to-cement ratios w/c of 0.35 and 0.40 were tested, whereas cement-to-sand ratio was kept constant at 0.50 by weight. The mechanical properties of the mortar were obtained by laboratory experiments, the Young's modulus was 28.1 GPa for mortar with $w/c = 0.35$ and 26.4 GPa for specimens with $w/c = 0.40$, and the Poisson's ratio was 0.22. The experiments were carried out by applying an increasing load force F at the mid-span, therefore the initial fracture propagated under mode I. A total of 20 configurations were tested, whose respective recorded maximum load forces are listed in Table 1. The plane-strain fracture toughness was computed afterward according to the ASTM E 399-12.

Our computational mesh is depicted in Fig. 3b. The central region of the beam is meshed by 4-noded regular square elements with size of 0.2 mm, and the

remaining domain by 3-noded unstructured triangular elements with maximum size of 1.25 mm, except in the supports where the maximum size is 0.8 mm. The total number of triangular elements is $20,930$ and square elements $18,090$. The beam is simply and rigidly supported. We assume plain strain condition, therefore the fracture energy is given by $g_c = K_{IC}^2(1-\nu^2)/E$. We apply the force load F adopting as a control parameter the vertical defection at the top mid-span point of the beam, and we stop the simulations when the fracture length is equal to 2/3 of the beam height. Self-weight is disregarded. An example of the contour plot of the phase-field variable is depicted in Fig. 3c, where the fracture is represented in red.

We simulate the 20 experiments reported in [47]. As in the previous simulations, run on the same machine, the computational time varies from 241 s to 700 s, which is directly related to the minimum time step that ranges from 2.0×10^{-4} s to 4.7×10^{-10} s respectively.

The maximum load forces and the relative errors between our simulations and the experimental results are listed in Table 1. The errors are lower to the 3%, which indicates that our phase field approach has a satisfactory accuracy to model the mortal cracking under mode I. The simulated critical loads are always larger than the experimental results, which agrees with the conclusion of *Ge et al.* [47]. We also plot the evolution of the load force against the vertical deflection of experiments 1 to 5 in Fig. 3d. The relationship between both variables is linear up to the critical load is reached, which is a characteristic behavior of brittle and quasi-brittle materials. Beyond this point, the fracture propagates very fast and deflection increases while the load decreases. This conclusion is in agreement with the experimental results.

4. Fracture propagation of gravity dams

We present two full-scale numerical examples in order to illustrate the ability of phase-field models to handle simplified practical situations. We apply our model to simulate the fracture propagation of gravity dams subjected to self-weight and hydrostatic load. The first example is the Koyna dam, widely used as a benchmark model. The second example is a theoretical gravity dam in which a fracture initiates and propagates in the upstream toe due to the hydrostatic load. The proposed method also aims to show the effect of water pressure inside the fracture on fracture propagation. We simplify the simulations by assuming that both concrete is modeled as an homogenous material, and flow inside fractures is laminar. In real situations, mass concrete contains rigid inclusions –rock aggregates– up to 150 mm in diameter and fractures tends to propagate around the aggregates. Moreover, if the fracture reaches a drain, flow inside the crack becomes turbulent, what has been disregarded in this study.

4.1. Koyna dam

Koyna dam is a 103 m gravity concrete dam located in India. It has been widely used as a benchmark model for seismic analysis [48, 49] and static analysis of fracture propagation due to overflow. *Gioia et al.* [50] employed this

dam to study the propagation of an initial horizontal fracture on the upstream face. They concluded that the most critical one is facing the change of slope on the downstream face. Subsequent studies have been undertaken by several authors through very unlike techniques, for instance *Ghrib and Tinawi* [51] adopted a continuous damage model, *Shi et al.* [52] used a discrete cohesive approach, *Roth et al.* [53] combined discrete X-FEM with continuous damage approaches, and *Dias et al.* [54] developed a discrete approach based on crack-path field and strain injection techniques.

The previous authors adopted the geometry and material properties of the dam reported in [55]. The cross section is depicted in Fig 4a, and the mechanical properties of the concrete are: Young's modulus 25 GPa, Poisson's ratio 0.2, Griffith critical energy release rate for mode I failure 100 Pa·m, and density 2450 kg/m^3. The initial fracture length is 10% of the thickness of the dam at its location. The applied loads were the self weight, the full reservoir hydrostatic load plus the overflow load. The reported analyses did not consider the mechanical effect of water pressure inside the fracture.

We study fracture propagation at Koyna dam through phase-field models. We adopt the same geometry, material properties and loads as in the previous studies. We also perform a sensibility analysis with respect to the mesh size, type of mesh, and length scale parameter ℓ. Our computational mesh is depicted in Fig 4b. The region of interest –a large enough area where the fracture propagates– is meshed with 4-noded structured squared elements and the remaining domain with 3-noded unstructured triangular elements. We study the effect of the mesh size over the fracture propagation by computing the model twice with two different mesh sizes in the region of interest, 4 cm –denoted as fine mesh– and 8 cm –coarse mesh–. We also study the effect of the mesh type –structured or unstructured– by meshing the region of interest with 3-noded unstructured triangular elements, as shown in Fig 4c, and we compute the model twice with the same two previous maximum sizes in the region of interest. The number and type of elements employed at each mesh are listed in Table 2.

We run the simulations on the same machine. The computational time of each simulation is listed in Table 2. It is approximately up to 6 times larger in the model with the finest meshes. Moreover, for the same size, the unstructured meshes are up to 3 times more demanding than the structured ones due to the larger number of elements.

The response of the structure is characterized by the overflow height versus the horizontal crest displacement in Fig 4d, as well as several contour plots of the phase-field variable. The fracture propagation is negligible for overflow heights lower than 6.7 m, and the crest displacement is linear with the overflow. Afterward, an extremely quick advance of the fracture occurs under a negligible load increase –snap-through–. After the unstable growth phase, the fracture continues to propagate as the load increases, but crest displacement is no longer linear with overflow. We run our simulations up to 10 m overflow level.

A good agreement is found between our computed response and the results reported in the literature, although some discrepancies with some authors are found during the unstable growth phase. While our model is able to simulate the

unstable phase maintaining a constant water level, in other works the overflow level decreases at the beginning of the phase and the fracture grows. Therefore, a local maximum in the overflow height versus displacement curve appears at the beginning of the phase. After the unstable phase, the results are quite similar.

We provide the contour plots of the phase-field variable for 10 m overflow level in Fig 4d. Red color indicates the damaged area, and it is the fracture pattern. The hydrostatic load generates compression on the downstream face and drives the fracture path downward and parallel to the downstream face. This pattern agrees quite well with the results reported in the literature.

We study the effect of the length scale parameter ℓ over the dam response in terms of overflow height versus crest displacement. We compute three models with ℓ varying from 0.2 to 0.4 m. The results are depicted in Fig 4d. The length scale parameter seems to have no effect on the dam response. However, the critical load, which triggers the unstable fracture propagation, slightly varies with ℓ: the load decreases as ℓ increases. This results is in accordance with the finding of other authors. For instance, *Vignollet et al.* [37] conducted several numerical experiments on an 1D bar subjected to a constant tensile loading and they found that the peak force decreased as ℓ increased. Since ℓ was introduced, in principle, as a mathematical parameter, the results of the numerical models reveal that it also behaves as an effective material parameter. This has already been pointed out by several authors such as [56, 25, 37].

Several contour plots of the phase-field variable are also included in Fig 4d. ℓ does not seem to have influence on these patterns, although the width of the damage area is larger as the parameter does. Since ℓ is a parameter which measures the band width where the regularization of the fracture surface takes place, the larger ℓ the wider damaged area.

We also perform a sensibility analysis with respect to the mesh size and type by analyzing the curves included in Fig 4e, together several contour plots of the phase-field variable. ℓ is 0.4 m in all the simulations. The coarse mesh has a maximum size of 8 cm and the fine 4 cm, the structured mesh is composed by square elements and the unstructured by triangles. The results are very similar for the four meshes. Slight differences are found in the critical load, which tends to be higher for the unstructured and coarse meshes. Moreover, the fracture patterns do not change with the mesh, at least qualitatively .

Finally, we study the fracture pattern for higher water levels. A new branch emerges, propagating towards the change of slope on the downstream face. *Jirásek and Zimmermann* [57] detected the formation of this second fracture, which has also appear in the cover of the book *Fracture and size effect in concrete and other quasi-brittle materials* by Z.P. Bazant and J. Planas –Fig 4f–. We provide the evolution of the overflow height versus the horizontal displacement in Fig 4g, in which we also include some contour plots of the phase-field variable at time steps of interest. The branching produces a new unstable growth phase in which the crest displacement suddenly grows whitout overflow increment –snap-through– . Thereafter, the fracture propagates further, but the slope of the evolution change and the resistence offered by the structure to the hydrostatic load is

lower.

4.2. Gravity dam without initial damage

This example deals with the initiation and propagation of a fracture in the upstream toe of a theoretical 2D plane-strain model of a gravity dam. We also describe a simple and straightforward way to consider the mechanical effect of water pressure inside the fracture, and we analyze the effect of the pressure over the final fracture length.

The geometry of the simulated dam is depicted in Fig 5a. The dam is 100 m height, the upstream face is vertical and the downstream slope is 0.75 : 1, and the crest is 2 m height and 4 m width. Concrete is depicted in blue and rock of the foundation in gray. The applied loads are the self weight and the hydrostatic load. The mechanical properties of the concrete are: Young's modulus 25 GPa, Poisson's ratio 0.25, Griffith critical energy release rate for mode I failure 120 Pa·m, and density 2400 kg/m^3, and the properties of the rock of the foundation are: Young's modulus 20 GPa, Poisson's ratio 0.25, and density 2500 kg/m^3. The region of interest –a large enough area where the fracture propagates– is meshed with 4-noded structured squared elements with size 1×10^{-4} m, and the remaining domain with 3-noded unstructured triangular elements. The mesh consists of $65,934$ triangular elements and $761,875$ square elements. The simulation is run on the same machine and requires $89,780$ s to solve all the time steps.

The water level in the reservoir increases with time, from 93 to 95.5 m. At level 94 m, a fracture initiates in the upstream toe and propagates. We plot the contour plot of the phase-field variable for the case where the mechanical effects of water pressure inside the fracture are not accounted for in Fig 5b and for the case where are considered in Fig 5c. The plots are zooms of the upstream toe –dashed rectangle of Fig 5a–. We assume the fracture does not reach any drain, as otherwise the flow along the fracture would become turbulent and the reported equation of fluid motion, Eq. (30), would no longer remain valid. We also assume that the fracture propagates in the toughness dominated regime, *i.e.*, the energy expended in fracturing the concrete in much larger than the viscous dissipation. In such case, the water pressure inside the fracture equals the hydrostatic load and there is no need to solve the governing equation of fluid motion inside the fracture. We also plot the fracture length versus the water level in the reservoir in Fig 5d for both cases.

The fracture patterns that arise is an essentially straight line in both simulations, although as the water level increases the path tends to turn and align vertically. The water pressure produces a longer fracture, approximately 10% more for the highest water level. Moreover, this effect is stronger as the fracture expands, since the pressure force over the fracture walls is higher as the crack is longer.

Both the phase-field approach and the J integral arise from the Griffith theory of brittle fracture. However, the classical J integral approach assumes a simply connected domain, no body forces in the solid, null stress along the fracture surface and that the crack propagates along its initial direction. Although

some assumptions are not strictly fulfilled in this example, the extremely small fracture length compared to the overall dimensions of the dam induces us to assume that the body forces and the shear effects leading to a possible mixed-mode fracture are negligible.

Accordingly, we compute the J integral for several fracture lengths at the upstream toe ranging from 0.100 to 2.00 m. We take the direction of the fracture from the results of the phase-field model. We do not account for mechanical effects of water pressure inside the fracture, and we consider the water level in the reservoir equals 95.5 m. For each assumed fracture length, we assess the J integral over several Γ paths, as shown in Fig. 5e, and the selected value is that which becomes path independent. The evolutions of both the J integral and the stress intensity factor K_I against the fracture length are depicted in Fig. 5f.

The phase-field model predicts a fracture of 0.115 m, and since $g_c = 120$ Pa·m the stress intensity factor K_I is 1.789×10^6 Pa·m$^{1/2}$. Nevertheless, for the same fracture length, the J-integral results into a $K_I = 3.215 \times 10^6$ Pa·m$^{1/2}$. The ratio between both is 1.80. There is a Configuration Correction Factor –CCF– between both methods around 1.80 that accounts for the difference between the results of the J integral and the phase field approaches. This CCF can be attributed on the one hand, to the fact that the loading is not canonical [58]. On the other hand, it may suggest the necessity to use a lower value of g_c in the phase field study. We can conclude that, for the case study, there is a CCF depending on the type of loading, size and geometry of both the fracture and the structural component, so that the value of the expected K_I obtained by the classical J integral approach match the sought results. The aforementioned CCF of 1.80 ranges within the usual values found in the literature for other configurations [58].

5. Conclusions

We have presented a computational framework for the simulation of fracture initiation and propagation in elastic media based on a phase-field approach. Our model is a quasi-static formulation for brittle fracturing based on continuum mechanics, energy minimization and thermodynamical principles. The approach includes an anisotropic degradation of the elastic energy which involves that fractures only propagate under tension. Moreover, our computational framework can account for mechanical effects of water pressure inside fractures. The result is a simple and straightforward formulation which can handle complex fracture patterns such as branching, joining, nucleation or kriging without any additional handling.

As far as we know, applications of phase-field models are mostly restricted to academic benchmarks, and the reported formulation has not been verified with experimental results. Phase-field models are not currently a true reliable alternative to simulate fracture propagation in real structures. This paper aims to show that phase-field models represent a competitive tool for engineering practice. For this purpose, we verify the model with two laboratory experiments

available in the literature and also apply the formulation to simulate fracture initiation and propagation in two full-scale concrete dams.

The first laboratory test investigates the two-dimensional propagation path of fractures in polymethyl methacrylate plates subjected to several biaxial loading states. Our numerical simulations match the experimental patterns. The second experiment studies the fracture of mortar beams subjected to three point bending tests. Our numerical results provide maximum load forces very similar to the experimental ones, with errors lower than 3%, and fracture patterns are successfully replicated.

The first full-scale numerical example is the propagation of a preexisting fracture in the upstream face of Koyna dam. Our results agree quite well with the simulations available in the literature. Moreover, we find that the larger values of the length scale parameter, the lower critical loads which triggers the fracture propagation. We also detect slightly higher critical loads for unstructured and coarse meshes. Fracture patterns qualitatively do not change with mesh type or size.

Our final example models the initiation and propagation of a fracture in the upstream toe of a gravity dam. We seek to elucidate whether the water pressure within the fracture is relevant or not, resulting into 10% longer fractures when water pressure is accounted for. For a given fracture length and hydrostatic load, we also compute the stress intensity factor through the classic J integral, and we compare to the value adopted in the phase-field model. We found a ratio between both equals 1.74, that we attribute on the one hand, to the fact that the loading is not canonical, and on the other hand, it may suggest the necessity to use a lower value of g_c in the phase field study. Nevertheless, this ratio ranges within the usual values found in the literature for other configurations.

Our research has shown a good performance of phase-field models to deal with laboratory experiments and academic structures. The main advantages of this approach, such as its ability to initiate, propagate or twist paths, have been shown. The key ability of the phase-field approach is the determination of the fracture path, even when branching occurs, efficiently and automatically without any additional handling. However, mesh size needs to be small enough to capture the physics and the characteristic lengths of the fracture phenomenon. Although the model has only been applied to a 2D problem, the method can be extended to 3D with more complex geometries and anisotropies without any modification of the formulation. We conclude that phase-field models are a promising alternative that deserves more research effort, so that it may be eventually employed to simulate fracture propagation in practical scenarios.

Acknowledgments

This research was supported by the Spanish Ministry of Economy and Competitiveness under grant CTM2014-54312-P. LCF also gratefully acknowledges funding from the Spanish Ministry of Economy and Competitiveness (grant RyC-2012-11704).

References

[1] Charles, J.A., and P. Tedd. *Lessons from historical dam incidents.* Environmental Agency, Bristol, UK, 2011.

[2] Altarejos-Garcia, L., I. Escuder-Bueno, A. Serrano-Lombillo, and M. Membrillera-Ortuño. Methodology for estimating the probability of failure by sliding in concrete gravity dams in the context of risk analysis. *Struct. Saf.*, 36-37:1–13, 2012.

[3] Santillán, D., E. Salete, D.J. Vicente, and M.Á. Toledo. Treatment of solar radiation by spatial and temporal discretization for modeling the thermal response of arch dams. *J. Eng. Mech.-ASCE*, 140(11):05014001, 2014.

[4] Santillán, D., E. Salete, and M.Á. Toledo A methodology for the assessment of the effect of climate change on the thermal-strain-stress behaviour of structures. *Eng. Struct.*, 92:123–141, 2015.

[5] Krueger, R. Virtual crack closure technique: history, approach, and applications. *Appl. Mech. Rev.*, 57(2), 109-143, 2004.

[6] Wangen, M. Finite element modeling of hydraulic fracturing on a reservoir scale in 2D. *J. Petrol. Sci. Eng.*, 77:274–285, 2011.

[7] Bouchard, P.O., F. Bay, and Y. Chastel. Numerical modelling of crack propagation: automatic remeshing and comparison of different criteria. *Comput. Meth. Appl. Mech. Eng.*, 192:3887–3908, 2003.

[8] Hillerborg, A., M. Modéer, and P.E. Petersson. Analysis of crack formation and crack growth in concrete by means of fracture mechanics and finite elements. *Cem. Concr. Res.*, 6(6):773–781, 1976.

[9] Möes, N., J. Dolbow, and T. Belytschko. A finite element method for crack growth without remeshing. *Int. J. Numer. Meth. Eng.*, 46:131–150, 1999.

[10] Liu, F., and R. Borja. A contact algorithm for frictional crack propagation with the extended finite element method. *Int. J. Numer. Meth. Eng.*, 76:1489–1512, 2008

[11] Oliver, J., A.E. Huespe, and P.J. Sánchez. A comparative study on finite elements for capturing strong discontinuities: E-FEM vs X-FEM. *Comput. Meth. Appl. Mech. Eng.*, 195:4732–4752, 2006.

[12] Wheeler, M.F., T. Wick, and W. Wollner. An augmented-Lagrangian method for the phase-field approach for pressurized fractures. *Comput. Meth. Appl. Mech. Eng.*, 271:69–85, 2014.

[13] Aranson, I.S., V.A. Kalatsky, and V.M. Vinokur. Continuum Field Description of Crack Propagation. *Phys. Rev. Lett.*, 85:118–121, 2000.

[14] Karma, A., D.A. Kessler, and H. Levine. Phase-field model of mode III dynamic fracture. *Phys. Rev. Lett.*, 87:045501, 2001.

[15] Eastgate, L.O., J.P. Sethna, M. Rauscher, T. Cretegny, C.S. Chen, and C.R. Myers. Fracture in mode I using a conserved phase-field model. *Phys. Rev. E*, 65:036117, 2002.

[16] Henry, H., and H. Levine. Dynamic Instabilities of Fracture under Biaxial Strain Using a Phase Field Model. *Phys. Rev. Lett.*, 93:105504, 2004.

[17] Karma, A., and A.E. Lobkovsky. Unsteady crack motion and branching in a phase-field model of brittle fracture. *Phys. Rev. Lett.*, 92:245510, 2004.

[18] Spatschek, R., E. Brener, and A. Karma. Phase field modeling of crack propagation. *Philosophical Magazine*, 91:75–95, 2011.

[19] Ambrosio, L., and V.M. Tortorelli. Approximation of functional depending on jumps by elliptic functional via Γ–convergence. *Comm. Pure Appl. Math.*, 43:999–1036, 1990.

[20] Mumford, D., and J. Shah. Optimal approximations by piecewise smooth functions and associated variational problems. *Comm. Pure Appl. Math.*, 42:577–685, 1989.

[21] Francfort, G.A., and J.J. Marigo. Revisiting brittle fracture as an energy minimization problem. *J. Mech. Phys. Solids*, 46:1319–1342, 1998.

[22] Bourdin, B., G.A. Francfort, and J.J. Marigo. Numerical experiments in revisited brittle fracture. *J. Mech. Phys. Solids*, 48:797–826, 2000.

[23] Ambati, M., T. Gerasimov, and L. De Lorenzis. A review on phase-field models of brittle fracture and a new fast hybrid formulation. *Comput. Mech.*, 55:383–405, 2015.

[24] Miehe, C., F. Welschinger, and M. Hofacker. Thermodynamically consistent phase-field models of fracture: Variational principles and multi–field FE implementations. *Int. J. Numer. Meth. Eng.*, 83:1273–1311, 2010a.

[25] Borden, M.J., C.V. Verhoosel, M.A. Scott, T.J. Hughes, and C.M. Landis. A phase-field description of dynamic brittle fracture. *Comput. Meth. Appl. Mech. Eng.*, 217:77–95, 2012.

[26] Hofacker, M., and C. Miehe. Continuum phase field modeling of dynamic fracture: variational principles and staggered FE implementation. *Int. J. Fract.*, 178:113–129, 2012.

[27] Hofacker, M., and C. Miehe. A phase field model of dynamic fracture: Robust field updates for the analysis of complex crack patterns. *Int. J. Numer. Meth. Eng.*, 93:276–301, 2013.

[28] Miehe, C., L.M. Schänzel, and H. Ulmer. Phase field modeling of fracture in multi–physics problems. Part I. Balance of crack surface and failure criteria for brittle crack propagation in thermo–elastic solids. *Comput. Meth. Appl. Mech. Engng.*, 294:449–485, 2015a.

[29] Miehe, C., M. Hofacker, L.M. Schänzel, and F. Aldakheel. Phase field modeling of fracture in multi–physics problems. Part II. Coupled brittle-to-ductile failure criteria and crack propagation in thermo–elastic–plastic solids. *Comput. Meth. Appl. Mech. Engng.*, 294:486–522, 2015b.

[30] Verhoosel, C.V., and R. De Borst. A phase-field model for cohesive fracture. *Int. J. Numer. Meth. Eng.*, 96:43–62, 2013.

[31] Mikelić, A., M.F. Wheeler, and T. Wick. A phase-field method for propagating fluid-filled fractures coupled to a surrounding porous medium. *Multiscale Model. Simul.*, 13:367–398, 2015a.

[32] Miehe, C., and S. Mauthe. Phase field modeling of fracture in multi-physics problems. Part III. Crack driving forces in hydro–poro–elasticity and hydraulic fracturing of fluid-saturated porous media. *Comput. Meth. Appl. Mech. Engng.*, 304:619–655, 2016.

[33] Abdollahi, A., and I. Arias. Phase-field modeling of fracture in ferroelectric materials. *Arch. Comput. Method Eng.*, 22:153–181, 2015.

[34] Kiendl, J., M. Ambati, L. De Lorenzis, H. Gomez, and A. Reali. Phase-field description of brittle fracture in plates and shells. *Comput. Meth. Appl. Mech. Eng.*, 312:374–394, 2016.

[35] Santillán, D., R. Juanes, L. Cueto-Felgueroso. Phase-field model of fluid-driven fracture in elastic media: immersed-fracture formulation and validation with analytical solutions. *J. Geophys. Res. Solid Earth* , In Press, 2017.

[36] Griffith, A.A. The phenomena of rupture and flow in solids. *Phil. Trans. Roy. Soc.*, A221:163–198, 1920.

[37] Vignollet, J., S. May, R. De Borst, and C.V. Verhoosel. Phase-field models for brittle and cohesive fracture. *Meccanica*, 49:2587–2601, 2014.

[38] Miehe, C. Comparison of two algorithms for the computation of fourth–order isotropic tensor functions. *Comput. Struct.*, 66:37–43, 1998.

[39] Mikelić, A., M.F. Wheeler, and T. Wick. A quasi-static phase-field approach to pressurized fractures. *Nonlinearity*, 28:1371–1399, 2015b.

[40] Miehe, C., M. Hofacker, and F. Welschinger. A phase field model for rate-independent crack propagation: Robust algorithmic implementation based on operator splits. *Comput. Meth. Appl. Mech. Eng.*, 199:2765–2778, 2010b.

[41] Garagash, D.I. Plane-strain propagation of a fluid-driven fracture during injection and shut-in: Asymptotics of large toughness. *Eng. Fract. Mech.*, 73(4):456–481, 2006.

[42] Hindmarsh, A.C., P.N. Brown, K.E. Grant, S.L. Lee, R. Serban, D.E. Shumaker, and C.S. Woodward. SUNDIALS: suite of nonlinear and differential/algebraic equation solvers. *ACM Trans. Math. Softw.*, 31(3):363–396, 2005.

[43] Irwin, G.R. Fracture strength of relatively brittle structures and materials. *J. Frankl. Inst.-Eng. Appl. Math.*, 290(6):513–521, 1970.

[44] Barsom, J.M.., and S.T. Rolfe. *Fracture and fatigue control in structures: applications of fracture mechanics.* ASTM, West Conshohocken, PA, USA, 1999.

[45] Rice, J.R. A path independent integral and the approximate analysis of strain concentration by notches and cracks. *J. Appl. Mech.*, 35:379–386, 1968.

[46] Thomas, A.L., and D.D. Pollard. The geometry of echelon fractures in rock: implications from laboratory and numerical experiments. *J. Struct. Geol.*, 15(3):323–334, 1993.

[47] Ge, Z., Y. Wang, Y. Hue, W. Sun, and R. Sun Evaluation of fracture in mortar subject to tension loading using phase field model and three point bending test. *Mater. Des.*, 86:121–128, 2015.

[48] Lee, J., and G.L. Fenves A plastic-damage concrete model for earthquake analysis of dams. *Earthq. Eng. Struct. Dyn.*, 27:937–956, 1998.

[49] Guanglun, W., O.A. Pekau, Z. Chuhan, and W. Shaomin Seismic fracture analysis of concrete gravity dams based on nonlinear fracture mechanics. *Eng. Fract. Mech.*, 65:67–87, 2000.

[50] Gioia, G., Z.P. Bazant, and B.P. Pohl. Is no-tension dam design always safe?–a numerical study. *Dam Eng.*, 3:23–34, 1992.

[51] Ghrib, F., and R. Tinawi. Nonlinear behavior of concrete dams using damage mechanics. *J. Eng. Mech.*, 121(4):513–527, 1995.

[52] Shi, M., H. Zhong, E.T. Ooi, C. Zhang, and C. Song. Modelling of crack propagation of gravity dams by scaled boundary polygons and cohesive crack model. *Int. J. Fract.*, 183(1):29–48, 2013.

[53] Roth, S.N., P. Léger, and A. Soulaïmani. A combined XFEM–damage mechanics approach for concrete crack propagation. *Comput. Meth. Appl. Mech. Eng.*, 283:923–955, 2015.

[54] Dias, I.F., J. Oliver, J.V. Lemos, and O. Lloberas-Valls. Modeling tensile crack propagation in concrete gravity dams via crack-path-field and strain injection techniques. *Eng. Fract. Mech.*, 154:288–310, 2016.

[55] Chopra, A.K., and P. Chakrabarti. The earthquake experience at Koyna dam and stresses in concrete gravity dams. *Earthq. Eng. Struct. Dyn.*, 1:151–164, 1972.

[56] Pham, K., H. Amor, J.J. Marigo, and C. Maurini. Gradient damage models and their use to approximate brittle fracture. *Int. J. Damage Mech.*, 20:618–652, 2011.

[57] Jirásek, M., and T. Zimmermann. Nonlocal rotating crack model with transition to scalar damage. In *Computational Plasticity*, Vol. 2. D.R.J. Owen, E. Oñate, and E. Hinton, eds., Int. Center for Numer. Meth. in Eng. (CIMNE), Barcelona, Spain, 1997.

[58] Ragab, A., and S. Bayoumi. *Engineering Solid Mechanics. Fundamentals and applications.* CRC Press, Boca Raton, FL, USA, 1999.

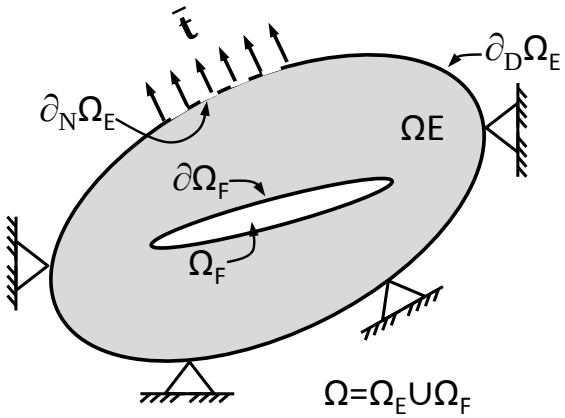

Figure 1: Diagram of the fluid-pressurized fracture domain Ω_F and elastic domain Ω_E.

Table 1: Experimental and numerical results of three point bending test on mortal specimens. Experimental results from [47].

Number of experiment	w/c	B(mm)	a(mm)	Failure load (N)		Difference
				Experiment	Simulation	%
1	0.35	40	10	1643.8	1664.4	1.25%
2	0.35	40	12.5	1408.8	1424.0	1.08%
3	0.35	40	15	1193.8	1203.9	0.91%
4	0.35	40	17.5	997.6	1002.0	0.44%
5	0.35	40	20	752.5	751.4	0.15%
6	0.35	20	10	673.5	682.3	1.31%
7	0.35	20	12.5	564.8	572.6	1.38%
8	0.35	20	15	514.3	520.1	1.13%
9	0.35	20	17.5	417.5	419.9	0.57%
10	0.35	20	20	322.0	322.0	0.00%
11	0.4	40	10	1373.8	1389.8	1.16%
12	0.4	40	12.5	1127.2	1143.5	1.45%
13	0.4	40	15	996.8	1009.5	1.27%
14	0.4	40	17.5	766.0	771.8	0.76%
15	0.4	40	20	628.5	628.1	0.06%
16	0.4	20	10	632.8	640.3	1.19%
17	0.4	20	12.5	530.5	538.2	1.45%
18	0.4	20	15	463.5	468.8	1.14%
19	0.4	20	17.5	386.1	396.5	2.69%
20	0.4	20	20	298.5	298.6	0.03%

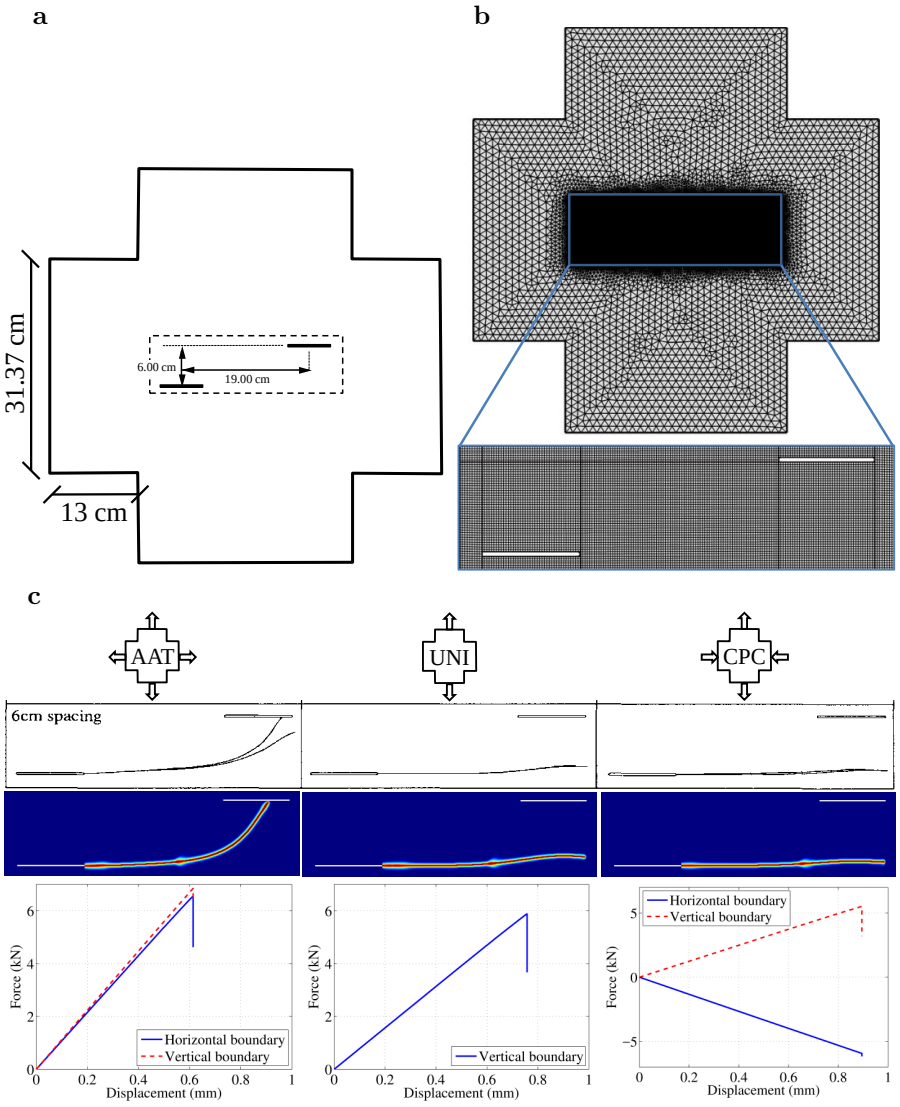

Figure 2: (**a**) Experimental method used to investigate fracture propagation. Lengths are in cm. A 4.5 mm thick cross shaped PMMA plate is subjected to imposed normal displacements at the arms of the cross. (**b**) Here we depict our computational mesh. (**c**) Fracture paths. We plot the loading combination in the first row, the experimental results from [46] in the second row, our numerical results in the third one, and the diagrams of force-deflections for numerical simulations –tension is positive–. The ratio of slot-parallel to slop-perpendicular applied displacements varies from 1 to 0 to -1, giving conditions of all-around tension (AAT), uniaxial loading (UNI), and crack-parallel compression (CPC).

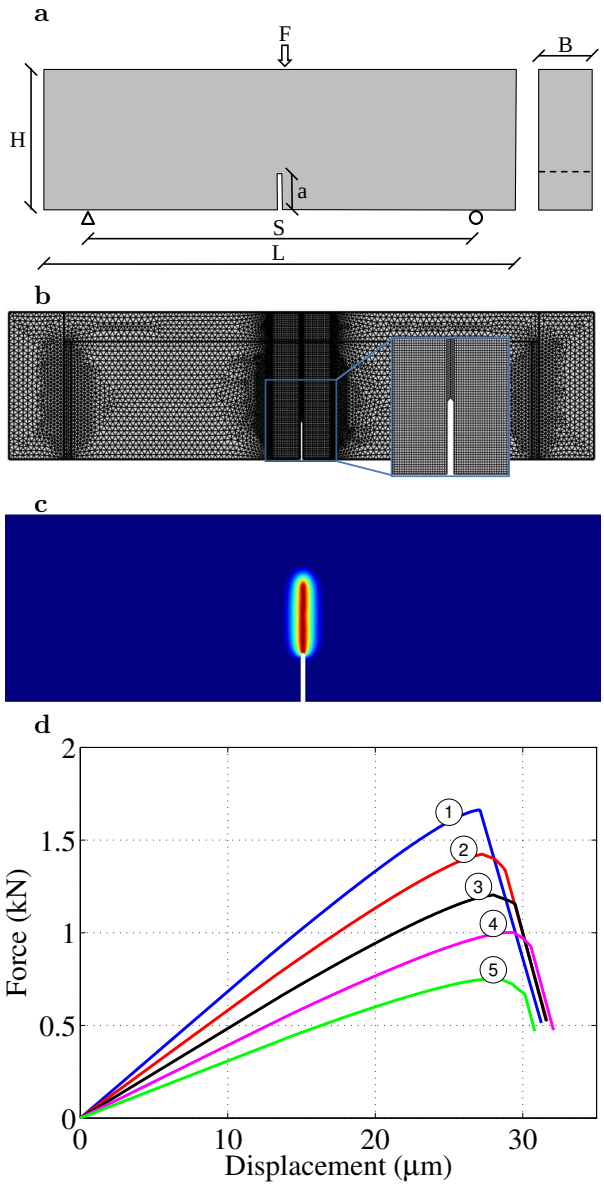

Figure 3: Three-point bending experiment and modeling results. (**a**) Schematic model setup. (**b**) Computational mesh. We also depict a close-up view of the structured mesh near the central region of the beam. (**c**) Phase-field variable, illustrating the fracture path, for the loading case 1. (**d**) Diagrams of force-vertical deflections for the numerical simulation of experiments 1 to 5.

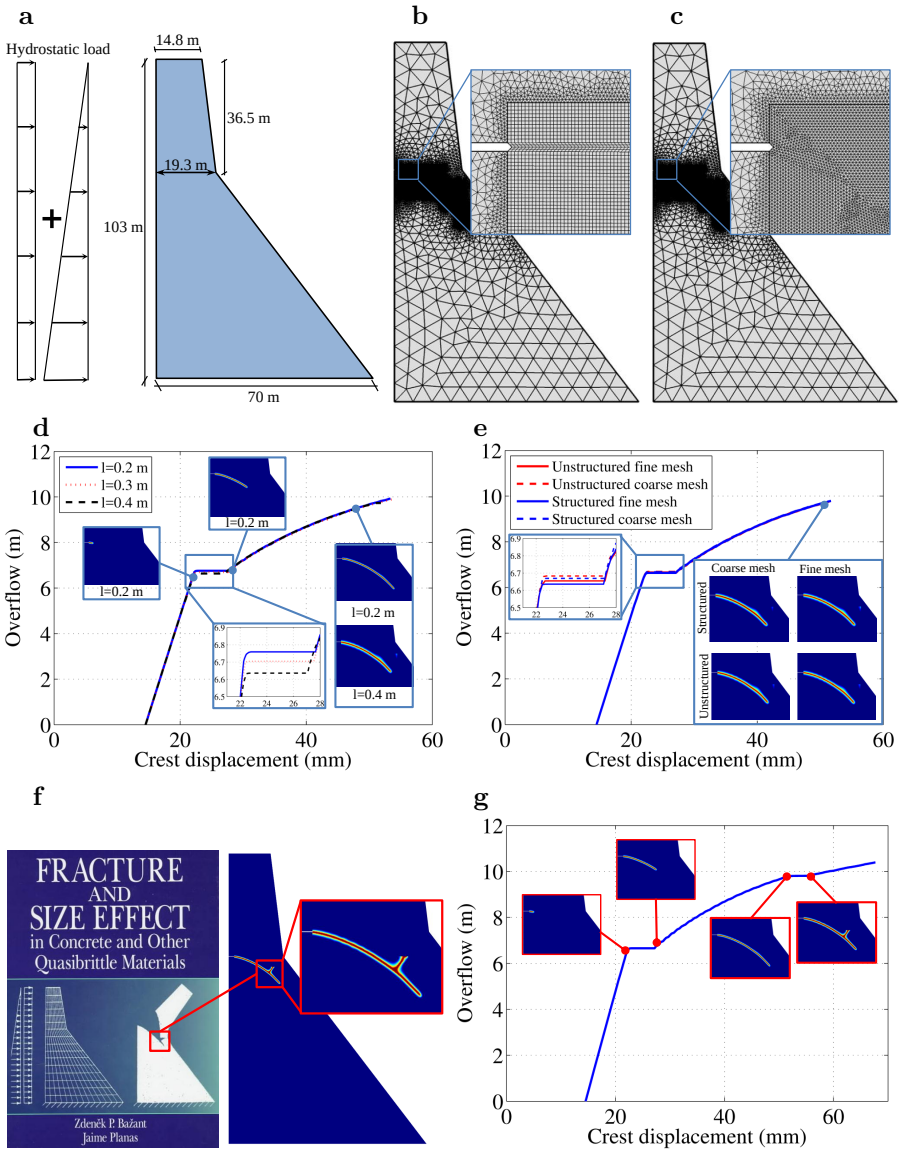

Figure 4: Phase-field analysis of the Koyna dam. (**a**) Model setup. (**b**)–(**c**) Computational mesh: (**b**) the refined mesh is composed of 4-noded structured squared elements, and (**c**) 3-noded triangular unstructured elements. (**d**), and (**e**) Plots of overflow against crest displacements. (**f**) Contour plot of the final phase-field and (**g**) plot of overflow against crest displacement.

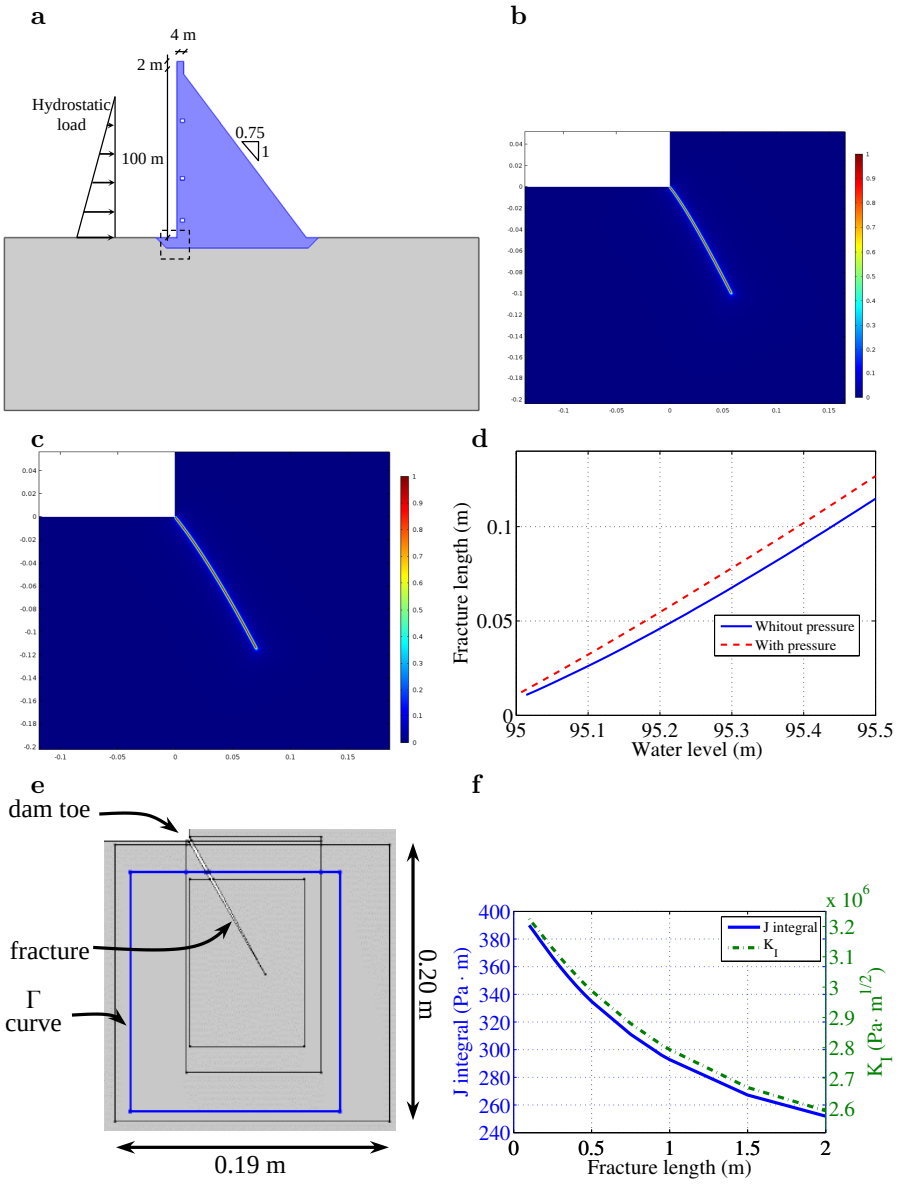

Figure 5: Phase-field analysis of a gravity dam without initial damage. (**a**) Model setup. (**b**)–(**c**) Contour plot of phase-field variable for the model: (**b**) without water pressure inside the pressure, and (**c**) with water pressure. (**d**) Fracture evolution. (**e**) Detail of the Γ curves around the fracture tip for assessing the J integral. (**f**) Evolution of J integral and K_I for several fracture lengths.

Table 2: Finite element grid resolutions used in the simulation of the Koyna dam, and total computing times.

Type of mesh	Number of elements		Computational
	triangular	square	time (s)
Unstructured fine mesh	$322,911$	0	$32,242$
Unstructured coarse mesh	$84,559$	0	$5,719$
Structured fine mesh	$26,987$	$106,375$	$11,885$
Structured coarse mesh	$13,196$	$27,022$	$2,930$